Supporting Information

Structural interconversions modulate activity of *E. coli* ribonucleotide reductase

Nozomi Ando[a,b,1], Edward J. Brignole[a,b,d,1], Christina M. Zimanyi[b], Michael A. Funk[b], Kenichi Yokoyama[b], Francisco J. Asturias[d], JoAnne Stubbe[b,c], and Catherine L. Drennan[a,b,c,2]

[a]Howard Hughes Medical Institute, [b]Department of Chemistry, and [c]Department of Biology, Massachusetts Institute of Technology, Cambridge, MA 02139

[d]Department of Cell Biology, The Scripps Research Institute, La Jolla, CA 92037

[1]These authors contributed equally to this work.

SI Methods.

Sample preparation. *E. coli* α_2 and β_2 were isolated as previously described (1, 2). To prevent substrate turnover and active site oxidation during experiments, β_2 was incubated with 30 mM HU (Sigma-Aldrich) at room temperature for 30 min to reduce the essential Y122 radical. α_2 was reduced by incubation with 30 mM 1,4-dithiothreitol (DTT, USB Corporation) for 30 min at room temperature, followed by incubation with 15 mM HU to reduce any trace β_2 that co-purifies with α_2. Both protein solutions were subsequently exchanged into assay buffer (50 mM HEPES pH 7.6 15 mM $MgCl_2$ 1 mM EDTA) by gel filtration with either a Superdex S-30 or Sephadex G-25 column and stored at –80 °C in 10-100 μL concentrated aliquots. The elution buffer was kept for the preparation of reference solutions for AUC and SAXS. The dimer concentrations of α_2 and β_2 were determined using ε_{280} of 189 and 131 $mM^{-1}cm^{-1}$, respectively; unless noted otherwise, all molar concentrations are dimer concentrations (i.e., α_2 or β_2). Pre-reduced α_2 had a specific activity of 2500 nmol/min/mg, and retained 97% activity after 11 h at room temperature, as determined by a coupled spectrophotometric assay (3). Prior to HU treatment, β_2 had a specific activity of 7700 nmol/min/mg and was shown to retain 92% activity after 11 h at room temperature. All of the experiments described here were performed with HU-treated β_2 and pre-reduced α_2.

Nucleoside 5′-diphosphates (NDPs) from Sigma-Aldrich were dissolved into water or assay buffer. The pH was slowly adjusted to 7-8 and the concentrations were determined spectroscopically using ε_{271} of 9.1 mM^{-1} cm^{-1} for cytidine and ε_{253} 13.7 mM^{-1} cm^{-1} for guanosine. High purity solutions of ATP, dATP, and TTP were purchased from USB Corporation. Nucleotide solutions were stored frozen in small aliquots and thawed immediately before experiments.

Analytical ultracentrifugation (AUC). Sedimentation velocity AUC was performed using a Beckman XL-I analytical ultracentrifuge at the MIT Biophysical Instrumentation Facility. Protein solutions and reference solutions were prepared with 5 mM DTT and the indicated final nucleotide concentrations, such that the buffer contents matched. Samples were injected in meniscus-matching cells outfitted with sapphire windows and interference window holders (Spin Analytical) and thermally equilibrated for several hours at 20.0 °C after radial calibration and adjustment of laser settings. Interference scans were collected at 40,000 rpm and 20 °C.

The apparent sedimentation coefficient distributions, $g(s^*)$, were generated using the time-derivative method implemented in the program DCDT+ (4) using 15-80 scans. To resolve high molecular weight species, the ranges of scans were chosen such that the peak broadening limit was at 540 kDa -1.3 MDa for complexes and 170 and 310 kDa, respectively for free subunits. In this method, differences in scan pairs collected within short time intervals approximate the time-derivatives of the sample concentration, dc/dt, from which $g(s^*)$ can be derived. The least-squared apparent sedimentation coefficient distributions, $ls\text{-}g^*(s)$, were obtained from the same sets of scans with whole boundary least squares fitting in Sedfit (5). s-values were corrected to standard values ($s_{20,w}$) using a solvent viscosity of 1.042 cp, solvent density of 1.00348 g/mL, and partial specific volumes as calculated in Sednterp (6) of 0.7335 and 0.7346 mL/g for α_2 and β_2, respectively. Molecular weights were determined by fitting Gaussians to isolated, concentration-independent peaks in $g(s^*)$ using DCDT+. Theoretical $s_{20,w}$ values of α_2, β_2, and $\alpha_4\beta_4$ were calculated with the program HYDROPRO (7) using the atomic coordinates from crystallography (4R1R (8), 1RIB (9), and this work) and molecular weights and partial specific volumes calculated from complete sequences in Sednterp (6).

Small-angle X-ray scattering (SAXS). SAXS was performed at the Cornell High Energy Synchrotron Source (CHESS) G1 station using a 10.5 keV 250 μm square X-ray beam with a

flux of several 10^{12} photons/s. Data were collected on a custom 1024x1024 pixel CCD detector (10) with a sample-to-detector distance of ~1.1 m. The transmitted intensity was measured on a PIN diode beamstop (11). Protein solutions and matching buffers were prepared following the same protocol used for AUC sample preparation and kept on ice until data collection. Samples were contained in 2 mm path length acrylic cells (ALine Inc.) (11) with 7.5 μm kapton windows (Chemplex). The same cell was used for acquisition of protein solution and background scattering pairs. Several 1 and 2 s exposures were taken per sample separated by 10 s pauses. The scattering images were corrected and integrated about the beam center following previously described image correction procedures (11). Exposures that did not display apparent radiation-induced changes were averaged and normalized by the transmitted intensities. Background scattering was subtracted from the protein solution scattering to produce the one-dimensional protein scattering profile, $I(q)$, as a function of q, where $q = 4\pi/\lambda \sin\theta$; 2θ is the scattering angle, and λ is the X-ray wavelength.

The pair distance distribution function, $P(r)$, was calculated from the experimental $I(q)$ with the indirect Fourier transform method (12) implemented in the program GNOM (13). The radius of gyration, R_g, and the forward scattering intensity, $I(0)$, presented in this article were determined from $P(r)$ by the relations:

$$R_g^2 = \frac{\int_0^{D_{\max}} P(r) r^2 dr}{2\int_0^{D_{\max}} P(r) dr} \text{ and}$$

$$I(0) = 4\pi \int_0^{\infty} P(r) dr,$$

where the maximum electron pair distance (i.e. maximum protein dimension), D_{max}, was chosen where $P(r)$ naturally approaches zero (12). Reasonable total estimate scores, as indicated by GNOM (13), were obtained in all cases.

Low-resolution models of protein structures were generated from the GNOM outputs

(with a high-resolution limit of $qR_g \sim 8$) using the *ab initio* reconstruction programs DAMMIF (14), DAMMIN (15), and GASBOR (16). The program, DAMAVER (17) was used to align *ab initio* models, reject outliers, and average the probable models. Theoretical scattering curves were calculated from atomic coordinates using CRYSOL (18). Singular value decomposition analysis and fitting of theoretical and experimental scattering curves to dATP titration data were performed using custom code written in MATLAB. Spline interpolation was used to match q values of the experimental and theoretical scattering curves. The $I(0)$ values of each species were scaled relative to each other by molecular weight and then adjusted to reflect the fixed protein content in the experiment. Linear combinations of scattering curves, $I_{fit}(q)$, were fitted to SAXS data using least-squares fitting in MATLAB:

$$I_{fit}(q) = c\sum_{i}^{N} f_i I_i(q),$$

where $I_i(q)$ and f_i are the scattering curve and molar fraction for the i-th species, N is the number of species, and c is a constant scaling factor.

Electron microscopy. 1.5 μM α_2 and β_2 were combined with 1 mM CDP and 0, 1, or 50 μM dATP in assay buffer. The mixture was incubated for 5 min at room temperature and then 5 μl of a 10-fold dilution in assay buffer with nucleotides was applied to a carbon coated 300 mesh Cu/Rh grid (Ted Pella) that had been glow discharged before use. The grid was immediately placed on a 45 μl drop of 2% uranyl acetate (Ted Pella) with 0.2% trehalose, then washed twice with 5 μl of the stain solution and a second carbon layer was applied (19).

Eighty-nine pairs of images of the -55° tilted and untilted specimen were collected at 50,000x magnification on a Tecnai F20 microscope (FEI) operated at 120 kV equipped with a 4096x4096 pixel CCD camera (Gatan). CCD images were corrected for background and gain during acquisition using Leginon (20) operated in manual mode. CCD frames have a pixel size

of 2.18 Å at the specimen level.

CCD frames were binned 4-fold for particle selection. EMAN2's e2boxer.py (21) was used in both Swarm and Manual modes to select ring- and C-shaped particles from the untilted images. Then for each tilted-untilted image pair, TiltPicker (22) was used to define the transform relating the images by selecting nine particles from the corners, edges, and center of the overlapping field in the tilted and untilted images. TiltPicker was modified to import the coordinates for the untilted particles and merge these with the already selected particles. After importing the e2boxer.py coordinates for the untilted image into TiltPicker, additional ring-like particles were selected and false positives pruned manually and then the coordinates were transferred to the tilted image.

A dataset of 14,055 tilt-pair particles were windowed from full-sized CCD images. Untilted particles were initially partitioned into 128 classes using “reference-free” alignment followed by rotationally invariant clustering (23) and used as references for an iterative alignment and classification routine (24, 25). Redundant class averages and those with poorly resolved features were then eliminated as references and 160 particles were removed from the dataset as members of 4 poor quality classes that emerged. Two classes that exhibited partial subunit occupancy were divided using correspondence analysis and hierarchical clustering. Finally, the iterative routine was used to refine the alignment and classification of the remaining 13,895 particles into 33 classes, 14 of which reveal fully formed $\alpha_4\beta_4$ rings (Fig. S6). Other averages indicate the presence of partially formed rings.

A 3D reconstruction was generated for the class of 1039 particles by back-projection of the tilted particles using Euler angles defined by the alignment parameters of the corresponding untilted particles (26). Prior to back-projection, the tilted particles were CTF corrected as

described by Radermacher (27) using scripts that were generously provided by T. Shaikh (Wadsworth Institute, Albany, NY). Because the 3D reconstruction was generated from a relatively small number of particles, 103 untilted particles in the class were randomly selected and included in the class reconstruction (28). Reconstructions were refined by four cycles of translational search and backprojection followed by three additional cycles that included a circumscribed optimization of in-plane (ψ) and projection angles (θ and ϕ). Because the α-β interactions appeared slightly asymmetric, no symmetry constraints were applied during refinement of the EM structure. The 3D EM density map was interpreted by rigid fitting crystal structures of α_2 (4R1R (8)) and β_2 (1RIB (9)) using UCSF Chimera (29). The individually fit α_2 and β_2 subunits and the $\alpha_4\beta_4$ crystal structure correspond closely to the contours of the EM map (Fig. 3B), except for some compression in the direction perpendicular to the plane of the EM specimen support. Compression is a well-documented artifact that often results from partial flattening of particles preserved in stain (30-33).

Crystallography. Crystallization was performed by hanging drop vapor diffusion using a protein sample that contained 25 μM α_2 (4.3 mg/mL) and 25 μM β_2 (2.2 mg/mL) in assay buffer supplemented with 5 mM DTT and 10 mM dATP. Protein solution (1 μL) was mixed with precipitant solution (1 μL) containing 100 mM MOPS pH 7.5, 12% PEG 3350, 300 mM magnesium acetate, 5% glycerol and 10 mM $FeCl_3$ and suspended over a 500 μL reservoir of precipitant solution. Crystals grew within 3 days at room temperature (~24°C). Crystals were cryo-protected by transferring briefly (3-4 s) to a solution of 100 mM MOPS pH 7.5, 12% PEG 3350, 200 mM magnesium acetate and 10% glycerol and then plunged directly into liquid N_2.

Data were collected on beamline 8.2.2 at the Advanced Light Source at the Lawrence Berkeley National Laboratory using an ADSC Quantum 315 CCD detector. Data were indexed and integrated with HKL2000 and scaled with Scalepack (34).

The structure was solved by molecular replacement using data to the full extent of the resolution in Phaser (35) and search models consisting of previously solved structures of α_2 and β_2 (2R1R chains A and B and 1MXR chains A and B, respectively) with all waters, ligands and ions removed. A solution with two α_2 and two β_2 molecules in the asymmetric unit was found.

Refinement was performed in CNS 1.3 (36) using all data with no sigma cutoff. Limited model building was performed in Coot (37). Refinement included rigid body, DEN assisted simulated annealing at 300 K (recently described for refinement of low resolution structures (38)), and restrained group B-factor refinement with one residue per group. Noncrystallographic symmetry (NCS) restraints were used, with one NCS group containing α chains A and B, a second group containing α chains C and D, and a third group containing all four β chains. The quality of the electron density map is shown in Fig. S8. All side chains were included in the model based on the high-resolution molecular replacement reference structures. Each of the four α chains contains residues 6-737 (of 761). Each of the four β chains contains residues 1-339 (of 375), and each contains some density for additional residues of the β C-terminal tail bound at the previously identified β tail binding site on α (39). C-terminal residues of β have been modeled at this site based on the previously solved structure of α_2 with peptide bound (2R1R). These residues include: 367-375 (β chains E, F), 363-375 (β chain G) and 365-375 (β chain H). Four dATP molecules per α_2 dimer were modeled at the known allosteric sites based on the orientation of bound nucleotides seen in previous structures (2R1R and 3R1R) and B-factors were refined (Fig. S8).

Table S1. Data collection and refinement statistics for crystal structure.

Data collection	
Beamline	Advanced Light Source Beamline 8.2.2
Space group	*C*2
Cell dimensions	
a, *b*, *c* (Å)	287.39, 153.46, 169.42
α, β, γ (°)	90.0, 119.91, 90.0
Wavelength (Å)	0.9794
Resolution (Å)[a]	50.0 – 5.65 (5.85-5.65)
Number of unique reflections	19134
R_{sym}	0.074 (0.599)
<I/σI>	9.3 (2.0)
Completeness (%)	99.4 (99.4)
Redundancy	3.1 (3.1)
Refinement	
Resolution	50.0 – 5.65
Number of unique reflections	19096
R_{work}/R_{free} (%)[b]	25.7/30.3
Number of atoms	
Protein	34781
dATP	240
Fe	8
Average *B*-factors (Å^2)	
Protein	242.2
dATP	290.5
Fe	120.0
R.m.s. deviations	
Bond lengths (Å)	0.004
Bond angles (°)	0.820
Ramachandran plot (%)	
Most favored (%)	90.3
Additionally allowed (%)	9.5
Generously allowed (%)	0.2
Disallowed (%)	0.0

[a]Highest resolution shell is shown in parentheses. [b]R_{free} was calculated using 5% of the data.

Table S2. SAXS shape reconstruction statistics from dATP titration experiment. All samples contained 1 mM CDP and were in 50 mM HEPES pH 7.6, 15 mM $MgCl_2$, 1 mM EDTA, 5 mM DTT. Experimental scattering profiles were converted into inputs for shape reconstructions in GNOM with reasonable total estimate scores (13). Ring-like states were reconstructed in DAMMIN with a cylindrical search space with the outer radius, inner radius, and height specified in parentheses; the averaged damstart model was used as a search space in a round of refinement (40).

	6 μM RNR	**6 μM RNR**	**6 μM RNR**	**6 μM RNR**
[dATP] (μM)	0	5	8	12
q range ($Å^{-1}$)	0.009-0.123	0.012-0.122	0.014-0.109	0.012-0.105
Real space range (Å)	0-164	0-192	0-200	0-200
Shape reconstruction	dammif 1.1.0	dammif 1.1.0	dammif 1.1.0	dammif 1.1.0
Symmetry	P1	P1	P1	P1
Search space	sphere	sphere	sphere	sphere
sqrt(χ^2)	1.794-1.796	1.913-1.916	1.721-1.723	1.757-1.760
# Models averaged/total	9/10	9/10	9/10	9/10
DAMAVER NSD (var)	0.570 (0.046)	0.518 (0.014)	0.625 (0.025)	0.780 (0.045)
	6 μM RNR	**6 μM RNR**	**6 μM RNR**	**3 μM RNR**
[dATP] (μM)	16	24	40	175
q range ($Å^{-1}$)	0.012-0.091	0.012-0.091	0.014-0.091	0.012-0.107
Real space range (Å)	0-205	0-186	0-200	0-198
Shape reconstruction	dammin53/fast	dammin53/fast	dammin53/fast	dammin53/fast
Symmetry	P1	P1	P1	P2
Search space (Å)	cyl(110,0,100)	cyl(110,0,100)	cyl(110,0,100)	cyl(110,20,100)
sqrt(χ^2)	1.391-1.394	1.371-1.376	1.303-1.309	1.900-1.904
# Models averaged/total	9/10	10/10	9/10	10/10
DAMAVER NSD (var)	0.589 (0.025)	0.589 (0.013)	0.665 (0.033)	0.796 (0.038)
Shape reconstruction	dammin53/slow	dammin53/slow	dammin53/slow	dammin53/slow
Symmetry	P1	P1	P1	P1
Refined search space	damstart	damstart	damstart	damstart
sqrt(χ^2)	1.392-1.394	1.369-1.371	1.304-1.305	1.899-1.901
# Models averaged/total	10/10	9/10	10/10	9/10
DAMAVER NSD (var)	0.450 (0.016)	0.421 (0.037)	0.537 (0.027)	0.471 (0.017)

Table S3. SAXS shape reconstruction statistics for the free subunits and the dATP-inhibited $\alpha_4\beta_4$ complex. All samples contained 1 mM CDP and were in 50 mM HEPES pH 7.6, 15 mM $MgCl_2$, 1 mM EDTA, 5 mM DTT. Experimental scattering profiles were converted into inputs for shape reconstructions in GNOM with reasonable total estimate scores (13). The $\alpha_4\beta_4$ ring was reconstructed in DAMMIN with a cylindrical search space with the outer radius, inner radius, and height specified in parentheses; the averaged damstart model was used as a search space in a round of refinement (40). Shape reconstruction of α_2 was performed in GASBOR with 1522 total residues.

	15 μM β_2	**15 μM α_2**
[dATP] (μM)	175	175
q range ($Å^{-1}$)	0.014-0.172	0.012-0.164
Real space range (Å)	0-81	0-121
Shape reconstruction	dammif 1.1.0	gasbor22i
Symmetry	P1	P2
Search space	prolate	sphere
sqrt(χ^2)	1.841-1.841	1.89-1.91
# Models averaged/total	10/10	9/10
DAMAVER NSD (var)	0.607 (0.032)	1.279 (0.222)

	1.5 μM $\alpha_4\beta_4$
[dATP] (μM)	175
q range ($Å^{-1}$)	0.012-0.107
Real space range (Å)	0-198
Shape reconstruction	dammin53/fast
Symmetry	P2
Search space (Å)	cyl(110,20,100)
sqrt(χ^2)	1.900-1.904
# Models averaged/total	10/10
DAMAVER NSD (var)	0.796 (0.038)
Shape reconstruction	dammin53/slow
Symmetry	P1
Refined search space	damstart
sqrt(χ^2)	1.899-1.901
# Models averaged/total	9/10
DAMAVER NSD (var)	0.471 (0.017)

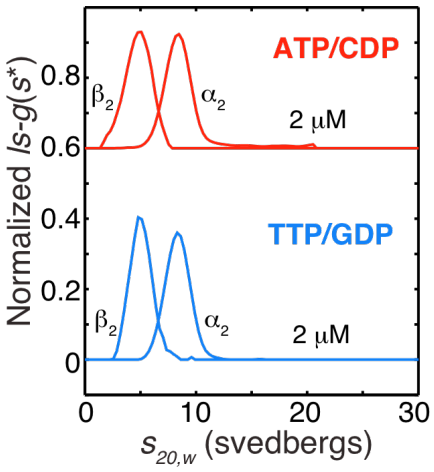

Fig. S1. Sedimentation coefficient distributions of individual subunits of *E. coli* class Ia RNR. In the presence of 3 mM ATP and 1 mM CDP (red curves) or 0.1 mM TTP and 1 mM GDP (blue curves), the individual subunits (each at 2 mM) sediment at approximately the theoretical values of 5.8 and 8.4 S determined from crystal structures (8, 9).

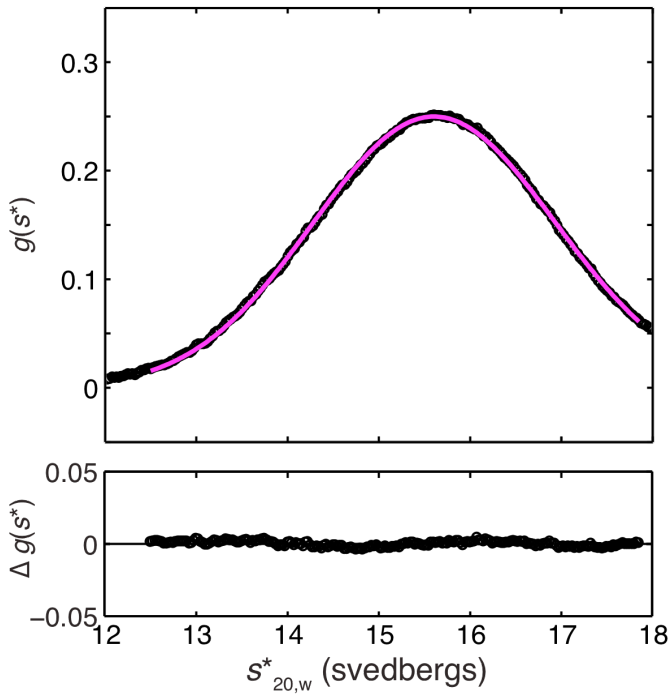

Fig. S2. Molecular weight determination of the dATP-inhibited complex by AUC. The apparent sedimentation coefficient distribution $g(s^*)$ at a low protein concentration of 2 μM (black) was chosen for Gaussian peak fitting to minimize the effects of non-ideality on molecular weight determination. A single species fit (magenta curve) was performed over the range 12.5 – 17.8 svedbergs in the program DCDT+ (4); the residuals, $\Delta g(s^*)$, have an r. m. s. value corresponding to 0.0076 fringes. The fit yielded a molecular weight of 533.2 (529.7, 536.4) kDa and an $s_{20,w}$ value of 15.632 (15.628, 15.635) svedbergs, where the 95% confidence intervals were calculated by the Monte Carlo method implemented in DCDT+.

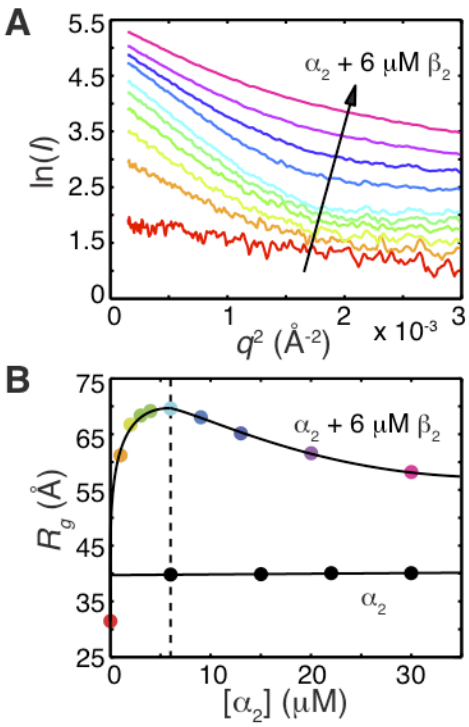

Fig. S3. Subunit stoichiometry revealed by SAXS titration in the presence of 175 μM dATP and 1 mM CDP. (A) Guinier representations of the scattering curves for the titration of 0-30 μM α_2 into a 6 μM β_2 (red to violet). The linear regions at low scattering angles (corresponding to length scales up to 630 Å) demonstrate the absence of non-specific aggregation in the samples. The change in slope as the titration continues indicates a change in the average radius of gyration, R_g. (B) Complex formation between 0-30 μM α_2 and a 6 μM β_2 (red to violet), as measured by R_g, is maximal at the equimolar point (dotted line), indicating a 1:1 subunit stoichiometry. The decrease in average R_g above the equimolar point can be attributed to the presence of excess α_2. Increasing the concentration of α_2 alone (black) does not result in higher order association.

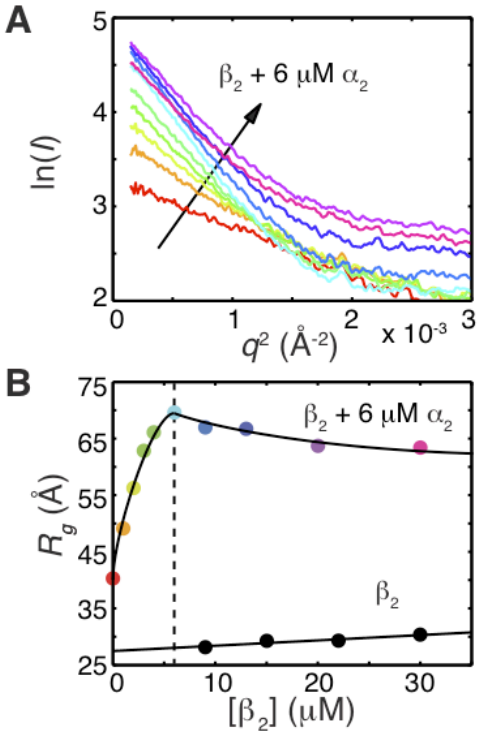

Fig. S4. Subunit stoichiometry revealed by SAXS titration in the presence of 175 μM dATP 1 mM CDP. (A) Guinier representations of the scattering curves for the titration of 0-30 μM β_2 into 6 μM α_2 (red to violet). The linearity at low scattering angles (corresponding to length scales up to 630 Å) demonstrates the absence of non-specific aggregation in the samples. The change in slope as the titration continues indicates a change in R_g. (B) Complex formation between 0-30 μM β_2 and 6 μM α_2 (red to violet), as measured by R_g, is maximal at the equimolar point (dotted line), indicating a 1:1 subunit stoichiometry. The decrease in average R_g above the equimolar point can be attributed to the presence of excess β_2. Increasing the concentration of β_2 alone (black) does not result in higher order association and has an R_g of 27.4 +/- 1.9 Å (SD) when extrapolated to zero protein concentration, in good agreement to that calculated from the dimeric crystal structure of 27.0 Å (9).

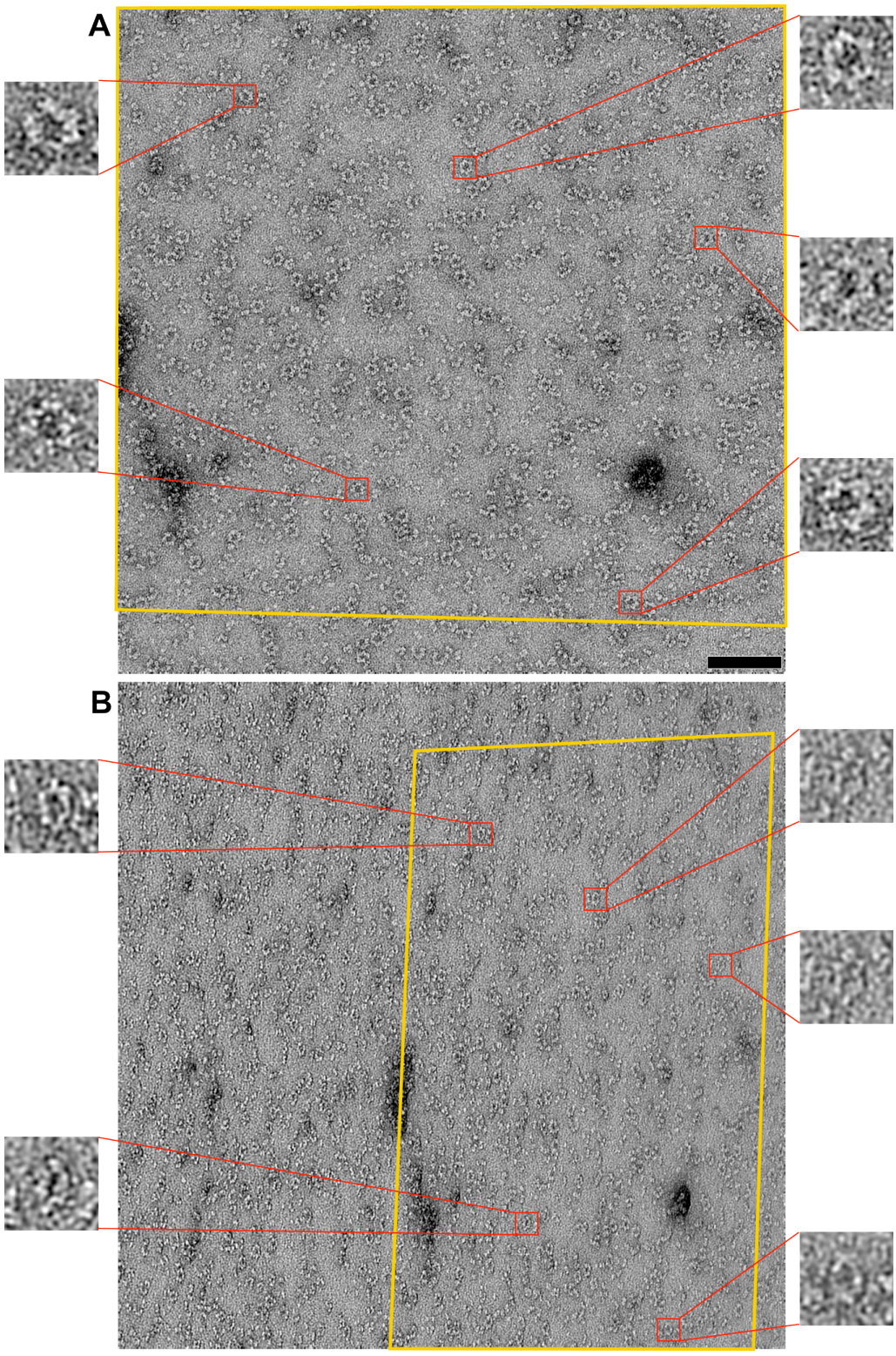

Fig. S5. Tilt pair EM images of negatively stained dATP-inhibited RNR. CCD images were recorded of the 0° (A) and -55° tilted (B) specimen of α_2 and β_2 prepared in the presence of 50 μM dATP and 1 mM CDP. Yellow trapezoids outline the overlapping region between the images. Individual ring-shaped particles such as those shown in the insets were selected for analysis. The scale bar in (A) corresponds to 1000 Å in the CCD frames or 250 Å in the insets.

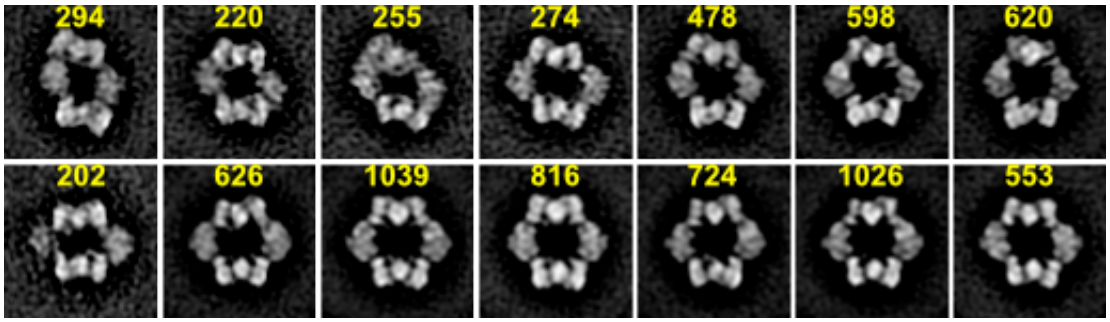

Fig. S6. Class averages determined from EM images of RNR in the presence of dATP. 13,895 particles were clustered into 33 classes that reveal differences in subunit stoichiometry and conformation. 14 class averages (56% of the particles) reveal fully formed $\alpha_4\beta_4$ rings (shown above). The number of particles in each class is indicated above its average.

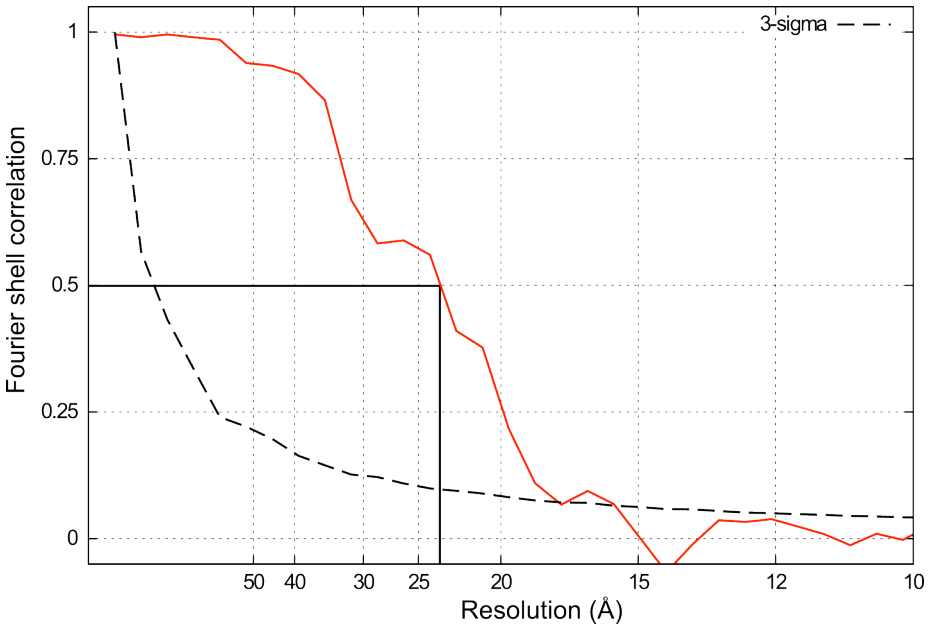

Fig. S7. Resolution of the $\alpha_4\beta_4$ EM reconstruction. Resolution for the 3D reconstruction of the class with 1039 particles (Fig. 3B) was estimated to be 23 Å using the 0.5 correlation criterion.

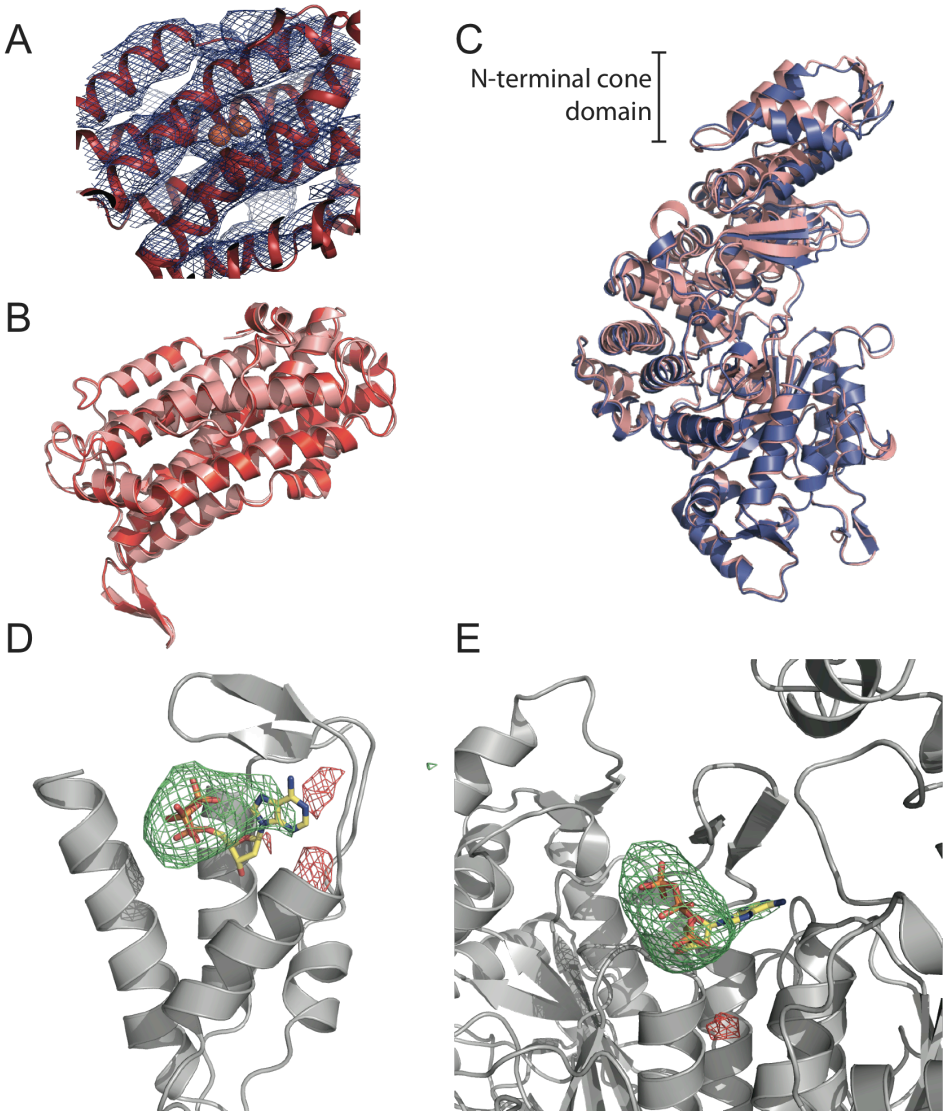

Fig. S8. Electron density and structure comparisons for the dATP-RNR crystal. (A) Electron density for one chain of a β_2 dimer is shown with a $2F_o$-F_c map at 5.65 Å resolution in blue mesh and contoured to 1.0 σ. Protein backbone is shown in red ribbons and two Fe atoms are shown as orange spheres. (B) An overlay of one β chain from the $\alpha_4\beta_4$ structure (in red) with β previously solved on its own (PDB ID 1PFR, in pink). The two chains overlay with no apparent differences. (C) An overlay of one α chain from the $\alpha_4\beta_4$ structure (in blue) with α previously solved on its own with AMP-PNP bound at the activity site (PDB ID 3R1R, in pink). The only differences appear to be in the N-terminal domain that houses the activity site. Because the structures being compared have different nucleotides bound we are unable to tell if these differences are due to the nucleotide, the presence of β or the error associated with low resolution data. (D) F_o-F_c density calculated when dATP is omitted at the activity site, contoured at +3.5 σ (in green) and -3.5 σ (in red). Despite the low resolution, there is a substantial positive electron density peak for dATP in this omit map. Protein backbone is shown as grey cartoons with nucleotides shown where they are modeled in the final structure as sticks with carbon in yellow, oxygen in red, nitrogen in blue, and phosphorus in orange. (E) F_o-F_c density calculated when dATP is omitted at the specificity site, contoured and colored as in (D).

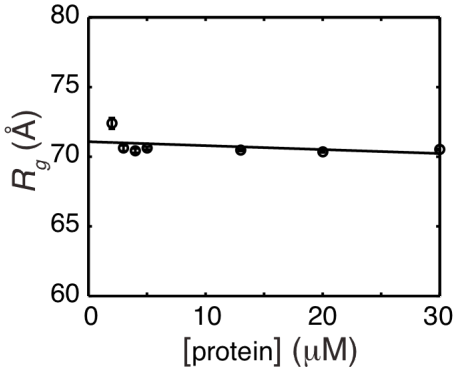

Fig. S9. Concentration independence of dATP-inhibited complex determined by SAXS. The R_g of equimolar solutions of α_2 and β_2 (2-30 μM) in the presence of 175 μM dATP and 1 mM CDP is concentration-independent over a wide range, indicating that the dATP-induced $\alpha_4\beta_4$ complex is stable and that larger oligomers do not form with increasing protein concentration. The R_g has a value of 71.1 +/- 1.1 Å (SD) when extrapolated to zero protein concentration to remove crowding and other inter-particle interaction effects.

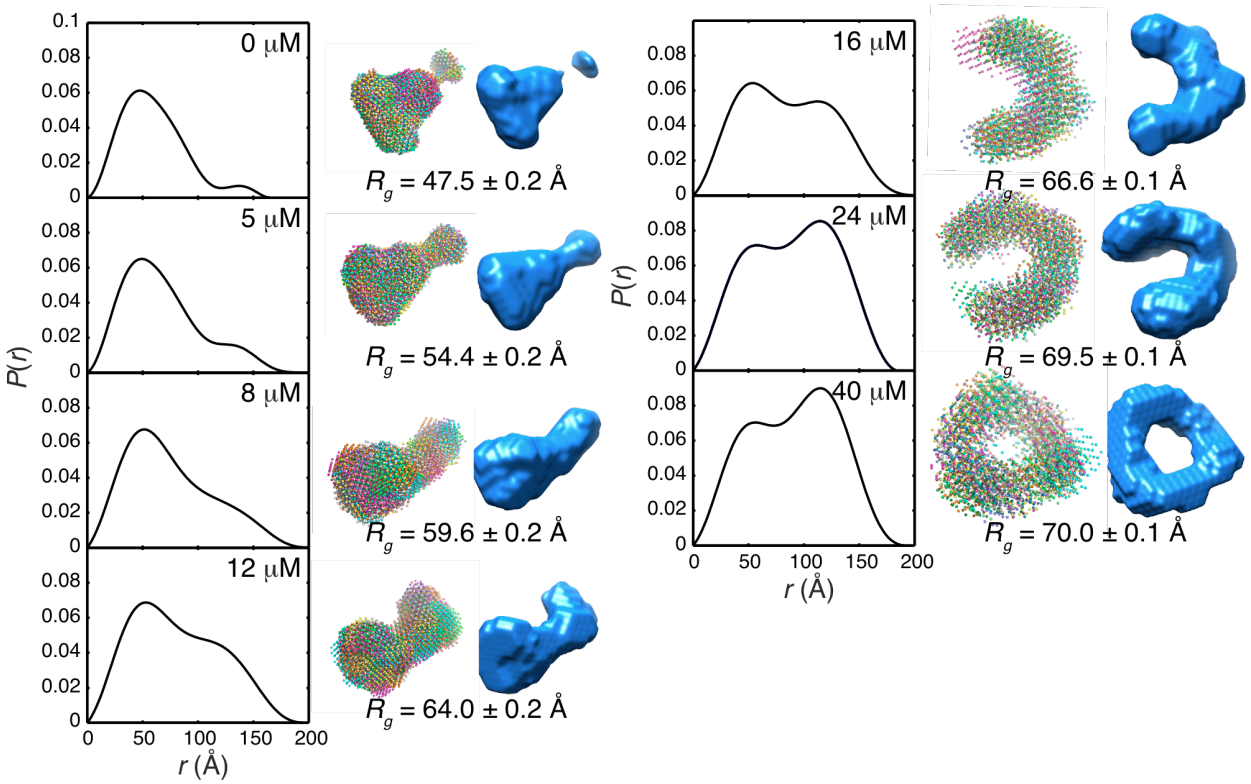

Fig. S10. SAXS titration of dATP (0-175 μM) into 6 μM solutions of α_2 and β_2 in the presence of 1 mM CDP. Pair distance distributions, $P(r)$, display the dATP-induced change in shape from a globular species to a non-globular species with a maximum dimension of 200 Å. The change in average shape can be visualized by three-dimensional *ab initio* shape reconstructions (statistics in Table S2). Individual DAMMIF (14) and DAMMIN (15) models are aligned and shown as bead models. The final averaged models generated by DAMAVER (17) are shown as blue surfaces. In the absence of dATP, the molecular envelope is largely globular and three-lobed, resembling the $\alpha_2\beta_2$ docking model (39). As dATP is titrated, the three-lobed mass reduces in size, and the additional density extends into a curved arm until an entire ring is formed. These shapes resemble averages of the two states in the dATP titration: the globular three-lobed $\alpha_2\beta_2$ and the dATP-inhibited $\alpha_4\beta_4$ ring.

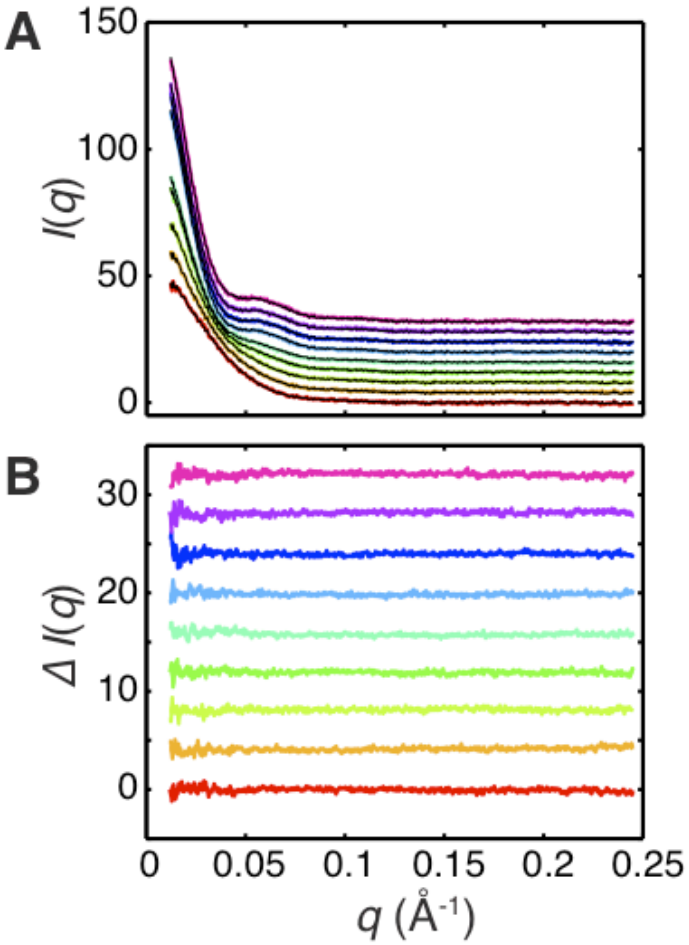

Fig. S11. SAXS titration of dATP (0-175 μM) into 6 μM solutions of α_2 and β_2 analyzed by singular value decomposition. (A) Linear combinations of the two major singular states (black curves) are nearly superimposable to the experimental data (red to violet correspond to increasing dATP concentration). (B) The residuals, $\Delta I(q)$, (same coloring as the scattering intensities) showed very little curvature, indicating that two states are sufficient to describe the data. For clarity, both the scattering intensities and residuals are plotted with constant offsets.

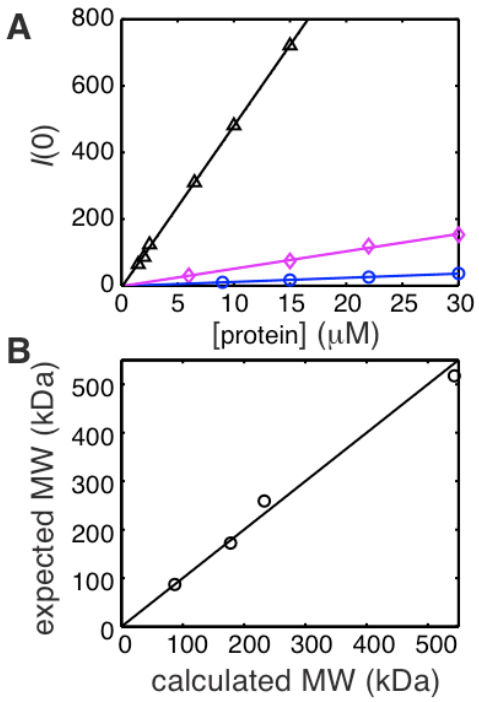

Fig. S12. Molecular weight determination by SAXS. At the dilute protein concentrations used in this study, the zero-angle scattering intensity $I(0)$ (i.e., $I(q)$ at zero scattering angle, or $q = 0$) is a function of protein molar concentration c, the electron density contrast between the hydrated protein and buffer $\Delta\rho$, and the excluded volume of the protein V_p, where the product $\Delta\rho \cdot V_p$ is approximately proportional to the molecular weight (12). Thus, $I(0) \propto c\ (\Delta\rho \cdot V_p)^2 \sim c\ \mathrm{MW}^2$. (A) The experimental $I(0)$ of β_2 alone (blue circles), α_2 alone (magenta diamonds), and $\alpha_4\beta_4$ (black triangles) in the presence of 175 μM dATP and 1 mM CDP were determined at multiple protein concentrations. $I(0)/c$ was determined from the slope, and MW was determined from the square root. (B) $I(0)/c$ from α_2 and β_2 were used as calibrants to convert $I(0)/c$ for $\alpha_4\beta_4$ and $\alpha_2\beta_2$ into molecular weights, where $I(0)/c$ of $\alpha_2\beta_2$was determined from 6 μM RNR in the presence of 1 mM CDP only. The expected and calculated molecular weights show a good correlation.

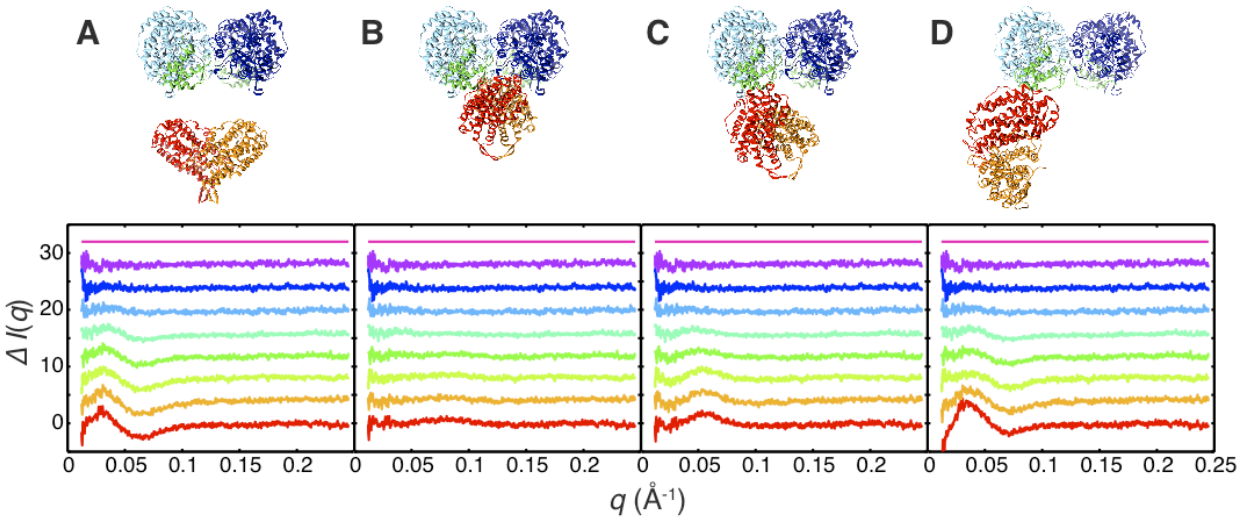

Fig. S13. Compact $\alpha_2\beta_2$ model best fits the initial state in the SAXS titration of dATP (0-175 μM) into 6 μM solutions of α_2 and β_2. Linear combinations of experimental scattering of the $\alpha_4\beta_4$ ring obtained at 175 μM dATP and theoretical scattering of (A) dissociated subunits (8, 9), (B) the $\alpha_2\beta_2$ docking model (39), (C) an asymmetric $\alpha_2\beta_2$ model generated by aligning *E. coli* subunit structures (8, 9) with the *S. typhimurium* class Ib structure (41), and (D) an open $\alpha_2\beta_2$ model representing half of the $\alpha_4\beta_4$ crystal structure were fit to the SAXS titration data in MATLAB. The residuals shown below each model (offset by a constant, with red to violet correspond to increasing dATP concentration) show the least curvature with the docking model; the residuals at 175 μM dATP (violet) are zero because the corresponding scattering curve was used to represent $\alpha_4\beta_4$ in the fitting.

SI References

1. Salowe SP & Stubbe J (1986) Cloning, overproduction, and purification of the B2 subunit of ribonucleoside-diphosphate reductase. *J. Bacteriol.* 165(2):363-366.
2. Salowe SP, Ator MA, & Stubbe J (1987) Products of the inactivation of ribonucleoside diphosphate reductase from Escherichia coli with 2'-azido-2'-deoxyuridine 5'-diphosphate. *Biochemistry* 26(12):3408-3416.
3. Yee CS, Seyedsayamdost MR, Chang MC, Nocera DG, & Stubbe J (2003) Generation of the R2 subunit of ribonucleotide reductase by intein chemistry: insertion of 3-nitrotyrosine at residue 356 as a probe of the radical initiation process. *Biochemistry* 42(49):14541-14552.
4. Philo JS (2006) Improved methods for fitting sedimentation coefficient distributions derived by time-derivative techniques. *Anal Biochem* 354(2):238-246.
5. Schuck P (2000) Size-distribution analysis of macromolecules by sedimentation velocity ultracentrifugation and lamm equation modeling. *Biophys J* 78(3):1606-1619.
6. Laue TM, Shah BD, Ridgeway TM, & L. PS (1992) *Computer-aided interpretation of analytical sedimentation data for proteins* (Royal Society of Chemistry, Cambridge).
7. Garcia de la Torre J (2001) Building hydrodynamic bead-shell models for rigid bioparticles of arbitrary shape. *Biophys Chem* 94(3):265-274.
8. Eriksson M, *et al*. (1997) Binding of allosteric effectors to ribonucleotide reductase protein R1: reduction of active-site cysteines promotes substrate binding. *Structure* 5(8):1077-1092.
9. Nordlund P & Eklund H (1993) Structure and function of the Escherichia coli ribonucleotide reductase protein R2. *J Mol Biol* 232(1):123-164.
10. Tate MW, *et al*. (1995) A Large-Format High-Resolution Area X-ray Detector Based on a Fiber-Optically Bonded Charge-Coupled Device (CCD). *Journal of Applied Crystallography* 28(2):196-205.
11. Ando N, Chenevier P, Novak M, Tate MW, & Gruner SM (2008) High hydrostatic pressure small-angle X-ray scattering cell for protein solution studies featuring diamond windows and disposable sample cells. *Journal of Applied Crystallography* 41(1):167-175.
12. Glatter O & Kratky O (1982) *Small angle X-ray scattering* (Academic Press, London ; New York) p 515 p.
13. Svergun D (1992) Determination of the regularization parameter in indirect-transform methods using perceptual criteria. *Journal of Applied Crystallography* 25(4):495-503.
14. Franke D & Svergun DI (2009) DAMMIF, a program for rapid ab-initio shape determination in small-angle scattering. *Journal of Applied Crystallography* 42(2):342-346.
15. Svergun DI (1999) Restoring low resolution structure of biological macromolecules from solution scattering using simulated annealing. *Biophys J* 76(6):2879-2886.
16. Svergun DI, Petoukhov MV, & Koch MHJ (2001) Determination of Domain Structure of Proteins from X-Ray Solution Scattering. *Biophysical Journal* 80(6):2946-2953.
17. Volkov VV & Svergun DI (2003) Uniqueness of ab initio shape determination in small-angle scattering. *Journal of Applied Crystallography* 36(3 Part 1):860-864.
18. Svergun D, Barberato C, & Koch MHJ (1995) CRYSOL - a Program to Evaluate X-ray Solution Scattering of Biological Macromolecules from Atomic Coordinates. *Journal of Applied Crystallography* 28(6):768-773.
19. Tischendorf GW, Zeichhardt H, & Stoffler G (1974) Determination of the location of proteins L14, L17, L18, L19, L22, L23 on the surface of the 50S ribosomal subunit of

Escherichia coli by immune electron microscopy. *Mol Gen Genet* 134(3):187-208.
20. Suloway C, *et al*. (2005) Automated molecular microscopy: the new Leginon system. *J Struct Biol* 151(1):41-60.
21. Tang G, *et al*. (2007) EMAN2: an extensible image processing suite for electron microscopy. *J Struct Biol* 157(1):38-46.
22. Voss NR, Yoshioka CK, Radermacher M, Potter CS, & Carragher B (2009) DoG Picker and TiltPicker: software tools to facilitate particle selection in single particle electron microscopy. *J Struct Biol* 166(2):205-213.
23. Penczek PA, Zhu J, & Frank J (1996) A common-lines based method for determining orientations for N > 3 particle projections simultaneously. *Ultramicroscopy* 63(3-4):205-218.
24. Brignole EJ & Asturias F (2010) Single-particle electron microscopy of animal fatty acid synthase: describing macromolecular rearrangements that enable catalysis. *Methods Enzymol* 483:179-202.
25. Brignole EJ, Smith S, & Asturias FJ (2009) Conformational flexibility of metazoan fatty acid synthase enables catalysis. *Nat Struct Mol Biol* 16(2):190-197.
26. Radermacher M, Wagenknecht T, Verschoor A, & Frank J (1987) Three-dimensional reconstruction from a single-exposure, random conical tilt series applied to the 50S ribosomal subunit of Escherichia coli. *J Microsc* 146(Pt 2):113-136.
27. Radermacher M, Ruiz T, Wieczorek H, & Gruber G (2001) The structure of the V(1)-ATPase determined by three-dimensional electron microscopy of single particles. *J Struct Biol* 135(1):26-37.
28. Fairman JW, *et al*. (2011) Structural basis for allosteric regulation of human ribonucleotide reductase by nucleotide-induced oligomerization. *Nat Struct Mol Biol* 18(3):316-322.
29. Goddard TD, Huang CC, & Ferrin TE (2007) Visualizing density maps with UCSF Chimera. *J Struct Biol* 157(1):281-287.
30. Kellenberger E, Haner M, & Wurtz M (1982) The wrapping phenomenon in air-dried and negatively stained preparations. *Ultramicroscopy* 9(1-2):139-150.
31. Boisset N, *et al*. (1990) Three-dimensional reconstruction of native Androctonus australis hemocyanin. *J Mol Biol* 216(3):743-760.
32. Cheng Y, *et al*. (2006) Single particle reconstructions of the transferrin-transferrin receptor complex obtained with different specimen preparation techniques. *J Mol Biol* 355(5):1048-1065.
33. Chandramouli P, Hernandez-Lopez R, Wang HW, & Leschziner AE (2011) Validation of the orthogonal tilt reconstruction method with a biological test sample. *J Struct Biol* 175(1):85-96.
34. Otwinowski Z & Minor W (1997) Processing of X-ray Diffraction Data Collected in Oscillation Mode. *Methods in Enzymology* 276(Macromolecular Crystallography, part A):307-326.
35. McCoy AJ, *et al*. (2007) Phaser crystallographic software. *J Appl Crystallogr* 40(Pt 4):658-674.
36. Brunger AT, *et al*. (1998) Crystallography & NMR system: A new software suite for macromolecular structure determination. *Acta Crystallogr D Biol Crystallogr* 54(Pt 5):905-921.
37. Emsley P, Lohkamp B, Scott WG, & Cowtan K (2010) Features and development of Coot. *Acta Crystallogr D Biol Crystallogr* 66(Pt 4):486-501.
38. Schroder GF, Levitt M, & Brunger AT (2010) Super-resolution biomolecular crystallography with low-resolution data. *Nature* 464(7292):1218-1222.

39. Uhlin U & Eklund H (1994) Structure of ribonucleotide reductase protein R1. *Nature* 370(6490):533-539.
40. Konarev PV, Petoukhov MV, Volkov VV, & Svergun DI (2006) ATSAS 2.1, a program package for small-angle scattering data analysis. *Journal of Applied Crystallography* 39(2):277-286.
41. Uppsten M, Farnegardh M, Domkin V, & Uhlin U (2006) The first holocomplex structure of ribonucleotide reductase gives new insight into its mechanism of action. *J Mol Biol* 359(2):365-377.